Laser Pulse Heating and Vapor Front Generation

B. S. Yilbas, S. Bin Mansoor, S. Z. Shuja, and H. Abualhamayel
ME Dept., KFUPM, Dhahran 31261, Saudi Arabia

DOI 10.1002/aic.11411
Published online January 24, 2008 in Wiley InterScience (www.interscience.wiley.com).

Laser nonconduction limited heating situation results in cavity formation and vapor front development above the cavity. As laser heating progresses, cavity wall recesses towards the solid bulk while the vapor front expands into its ambient due to recoil pressure generated at liquid-vapor interface in the cavity. To obtain velocity, temperature, and pressure fields in the evaporating front become challenging, since the process involves with transient evaporation of the surface during the absorption of the laser energy by the solid substrate. In the present study, phase change processes taking place in the substrate material during a laser heating process are modeled using an energy method and evaporating front behavior is modeled using the transient flow equations. Since the problem is involved with the multi-physics, the numerical technique is introduced to solve the resulting governing equations. The water ambient is assumed around the cavity in order to resemble the laser processing situation, particularly for laser shock processing. It is found that for nanosecond pulses with high intensity, the recession velocity of the surface reaches about 100 m/s at the symmetry axis and the recoil pressure of in the order of 10 GPa is generated in the cavity as a result of rapid evaporation. © 2008 American Institute of Chemical Engineers *AIChE J,* 54: 627–638, 2008

Keywords: laser, pulse, heating, phase change, cavity, vapor

Introduction

Lasers are widely used in industry as a machine tool. Proper selection of the laser and workpiece parameters is important to ascertain a good end product quality. Experimentation on parameter selection is timely and costly. To minimize the experimental effort and increase the knowledge on the physical processes taking place during laser machining, model studies become fruitful. To achieve a realistic simulation of the process, actual physical parameters as well as less model simplifications are necessary. However, mass removal via evaporation limits the realistic simulation situation, since vapor state properties of metallic substrates are not known in the open literature. Consequently, in model studies one of the approaches is to assume metal vapor properties in the simulations and obtain the qualitative information on the process.

Considerable research studies were carried out to explain laser evaporative heating process. High intensity laser induced evaporation and explosion of solid material were investigated by Dabby and Paek.[1] They indicated that once the temperature below the evaporated surface exceeds the temperature at the surface, explosive removal of material took place, which in turn led to high rate of mass removal rate from the surface. High power laser interaction with solid and formation of plasma were studied by Bech et al.[2] They indicated the ambient gas composition had significant effect on the plasma characteristics. Laser-induced plasma generation during pulsed irradiation of a laser beam was examined by Lacroix et al.[3] They indicated the Nd:YAG beam absorption of plasma was weak. The modeling of laser induced ablation of the solid surface due to laser irradiation pulse

Correspondence concerning this article should be addressed to B. S. Yilbas at bsyilbas@fupm.edu.sa.

was carried out by Liu et al.[4] They assumed isotropic expansion of the vapor front and predicted the vapor jet expansion into the ambient stagnant fluid. High power laser induced interaction with the solid surface was considered by Semak and Matsunawa.[5] They predicted the recoil pressure at the cavity surface during the ablation process. A study on the evaporating surface and vapor formation during laser irradiation pulse was carried out by Szymanski et al.[6] They indicated that the plumes above the cavity consisted of metal vapors diluted by ambient gas. The phase change processes during laser heating process was formulated by Zhang and Faghri.[7] They predicted the depth of cavity and liquid zone. In addition, they indicated that the conduction heat loss reduced significantly with increasing liquid layer thickness. The gas-dynamics model for laser ablation was considered by Gusarov et al.[8] They used an enthalpy method to predict the depth of evaporated region; however, recoil pressure calculations were simplified via using one-dimensional form of governing equations.

Material evaporated from the solid surface during the heating process, as ejected into its ambient, forms a jet emerging from the cavity. Although the size of the cavity is considerably small, jet velocity is very high due to high rate of mass removal during the evaporation process. In this case, flow field in the jet becomes turbulent and mixing of ambient fluid, with the emerging jet, particularly in jet boundary forms a complicated flow filed. This situation requires the turbulence modeling and species transfer analysis for the emerging jet. Consequently, turbulence affect and mixing of the emerging jet become essential to accommodated in the model study. Considerable studies were carried out to investigate unsteady turbulent jets. Spreading rate and penetration depth of an unsteady turbulent jet were studied by Kouros et al.[9] They showed that spreading rate was independent of jet velocity and spraying rate of unsteady jet is half of that corresponding to the steady jet. The entrainment characteristics of transient gas jets were examined by Abraham.[10] He indicated that the entrainment rate scaled linearly with axial penetration and total mass entrained had a cubic dependence on axial penetration of the gas jet. The influence of ambient pressure on turbulent vertical jets and plumes was investigated by Riopelle et al.[11] They showed that slight variation in ambient pressure distribution affected the jet and plume developed significantly. Turbulent transient gas injection was simulated by Ouellette and Hall.[12] They used k-ε model to account for the turbulence and indicated that k-ε model could correctly represent experimental data on jet penetration.

In the present study, vapor jet emerging from the laser produced cavity and its expansion above the cavity are examined. The recession of the solid surface is formulated using the energy method while a control volume approach is introduced when solving transient flow equations for the jet expansion. The k-ε turbulence model is accommodated to account for the turbulence. A stagnant water is assumed for the expanding jet ambient.

Mathematical Analysis of Heating and Transiently Developing Vapor Jet

Phase change process

When high intensity laser beam interacts with the solid surface, solid heating and phase change processes take place.

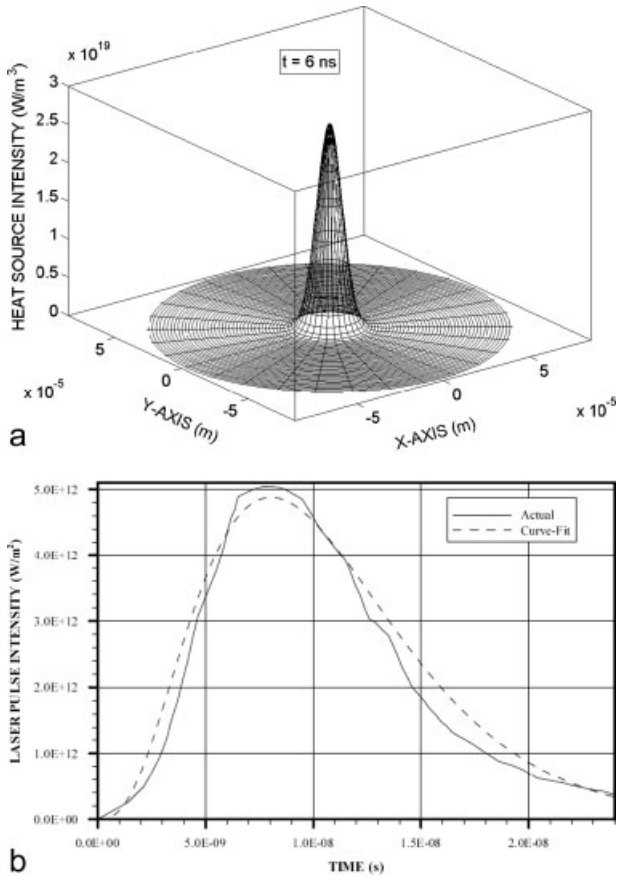

Figure 1. (a) Spatial distribution of laser pulse intensity at the surface of the substrate material after 6 ns; (b) temporal variation of laser pulse intensity.

Laser pulse intensity distribution resembling the actual laser pulse.

To model such heating situation, energy equation for each phase needs to be solved independently and they should be coupled across the interfaces of the regions where two-phases exist (mushy zones). The laser output power intensity distribution at the workpiece is assumed to be a Gaussian and its spot centre is at the centre of the co-ordinate system is considered (Figure 1a) while the temporal variation of laser power intensity resembling the actual laser pulse is shown in Figure 1b. This arrangement results in an axisymmetric heating of the substrate material.

In the initial stage, the conduction heating of the solid substrate with convective boundary condition at the surface can be considered. This is due to that the pulse duration is short and the radiation losses from the surface are negligibly smaller than the internal energy gain of the substrate material during heating.[13,14] Consequently, the heat transfer equation for a solid phase heating due to a laser irradiation pulse with a Gaussian intensity profile can be written as

$$\rho_s C_{p_s} \frac{\partial T}{\partial t} = \frac{k_s}{r} \frac{\partial}{\partial r}\left(r \frac{\partial T}{\partial r}\right) + k_s \frac{\partial^2 T}{\partial z^2} + S_o \qquad (1)$$

where S_o is the volumetric source term and it is,

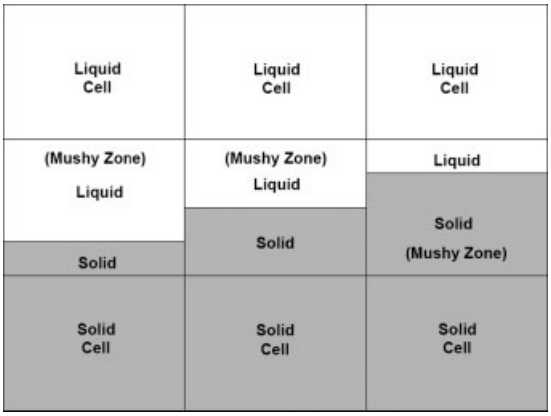

Figure 2. Temporal variation of laser pulse intensity.

A schematic view of the mushy zone.

$$S_o = I_o \delta (1 - r_f) \exp(-\delta z) \exp\left(-\frac{r^2}{a^2}\right)$$

I_o, δ, r_f and a are the laser peak power intensity, absorption coefficient, reflectivity, and the Gaussian parameter, respectively. Since the heating problem is transient, the initial condition should be defined, i.e., initially it is assumed that the substrate material is at a uniform temperature, which can be specified. Therefore,

$$\text{At time zero} \Rightarrow t = 0 : T(r, z, 0) = T_o(\text{specified})$$

Because of the short duration of laser pulse, insulated boundary is assumed at the surface and at a distance considerably away from the surface (at infinity). Since the heating has no effect on the temperature rise at a depth of infinity below the surface, temperature is assumed to be constant and equals to the initial temperature of the substrate material in this region. The boundary conditions, therefore, are

$$z \text{ at infinity} \quad \Rightarrow \quad z = \infty : T(r, \infty, t) = T_o(\text{specified})$$

$$r \text{ at infinity} \quad \Rightarrow \quad r = \infty : T(\infty, z, t) = T_o(\text{specified})$$

$$\text{At symmetry axis} \quad \Rightarrow \quad r = 0 : \frac{\partial T(0, z, t)}{\partial r} = 0$$

$$\text{At the surface} \quad \Rightarrow \quad z = 0 : \frac{\partial T(r, 0, t)}{\partial z} = h(T(r, 0, t) - T_o)$$

where h is taken as 10 W/m^{2}K due to natural convection from the surface.[13]

It is assumed that the substrate material has single melting and boiling temperatures. To accommodate the phase change process, heat transfer equation for solid heating is modified and an energy method can be used. Once the phase change initiates, a mushy zone (partially solid and partially liquid or partially liquid and partially vapor) can be generated across the interface where the phase change occurs (Figure 2). During the phase change process, including the mushy zone, temperature of the substrate material remains the same, but its enthalpy changes in this region, which can be formulated after considering the energy balance in the mushy zone. Consider a differential element in a substrate material (Figure 2), which is in the mushy zone and let x_m be the mass fraction of liquid present in the element, then the energy content (ΔU) of the differential element with volume ΔV at melting temperature T_m can be written as

$$\Delta U = \rho_m \Delta V \left[x_m \left(L_m + c_{p_m} (T_m - T_{ref}) \right) + c_{ps} (1 - x_m)(T_m - T_{ref}) \right] \quad (2)$$

where,

$$x_m = \frac{m_m}{m_m + m_s}$$

T_{ref}, x_m, m_m, m_s are reference temperature for enthalpy, quality of liquid, mass of liquid, and mass of solid in the element, respectively. After assuming specific heat of melt is the same as the solid at melting temperature ($c_{p_s} = c_{p_m}$ at $T = T_m$), then Eq. 2 reduces to

$$\Delta U = \rho_m \Delta V \left[x_m L_m + c_{p_m} (T_m - T_{ref}) \right] \quad (3)$$

For per unit volume, it reduces to

$$\frac{\Delta U}{\Delta V} = \Delta u = \rho_m \left[x_m L_m + c_{p_m} (T_m - T_{ref}) \right] \quad (4)$$

Differentiation with time yields

$$\frac{\partial u}{\partial t} = \rho_m L_m \frac{\partial x_m}{\partial t} \quad (5)$$

since $c_{p_m}(T_m - T_{ref}) = \text{const.}$

Substituting Eq. 5 into Eq. 1 gives the energy equation for the differential element subjected to a phase change process

$$\rho_m L_m \frac{\partial x_m}{\partial t} = \frac{k_m}{r} \frac{\partial}{\partial r} \left(r \frac{\partial T}{\partial r} \right) + k_m \frac{\partial^2 T}{\partial z^2} + S_o \quad (6)$$

Equation 6 is applicable for the differential elements in the mushy zone when temperature reaches melting temperature of substrate material ($T = T_m$) and $0 \leq x_m \leq 1$. Conse-

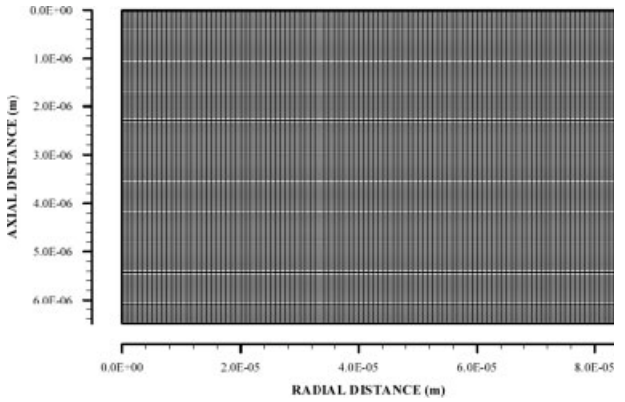

Figure 3. A mesh used in the simulations for heat transfer.

quently, temperature of the cells with $0 \leq x_m \leq 1$ is set to melting temperature $T = T_m$. When the value of x_m exhibit 1 ($x_m > 1$), Eq. 6 is not applicable for the differential element under consideration in the mushy zone. In this case, Eq. 1 is used to determine the temperature rise in the liquid heating with accommodating the liquid thermal properties in the equation. Moreover, the liquid heating continues until the boiling point is reached in the substrate material.

In the case of boiling of the substrate material, a new mushy zone is created. In this case, Eq. 6 can be modified for a differential element under going evaporation, i.e.

$$\rho_b L_b \frac{\partial x_b}{\partial t} = \frac{k_b}{r}\frac{\partial}{\partial r}\left(r\frac{\partial T}{\partial r}\right) + k_b\frac{\partial^2 T}{\partial z^2} + S_o \tag{7}$$

Equation 7 is applicable for the range $T = T_b$ and $0 \leq x_b \leq 1$ in the mushy zone (partially liquid partially vapor zone). Consequently, temperature of the cells with $0 \leq x_b \leq 1$ is set to boiling temperature ($T = T_b$). It should be noted that x_m is replaced with x_b in Eq. 5, which represents the fraction of vapor phase in the differential element. The calculation of x_b is the same as x_m, provided that latent heat of fusion is replaced with latent heat of evaporation of the substrate material in Eq. 5 in the later.

The boundary condition at the evaporating surface is introduced in relation to Eq. 7. In this case, the temperature along the evaporated surface is kept at boiling temperature of the substrate material, i.e., the cells in the evaporated region are kept at boiling temperature, i.e.

In the mushy zone, at $z = z_b \Rightarrow T(r, z_b, t) = T_b$ where z_b represents the axial location at the evaporated surface.

Equations 6 and 7 enable us to determine the relative position of solid-liquid and liquid-vapor interface in the substrate material. Liquid-vapor interface determines the shape and size of the cavity generated during evaporation process.

Transiently Developing Vapor Jet

The vapor jet emanating from the laser produced cavity is modeled numerically using a control volume approach. The laser produced cavity shape and its temporal development are employed in the simulations. In this case, the time-varying cavity shape, mass flux of the vapor and the temperature distribution at the cavity surface are the inputs for the simulations. In order to model such flow situation, the fluid dynamic/mass transfer model is accommodated in the analysis. In the analysis the Reynolds Averaged Navier-Stokes equations comprising of the continuity equation, the radial and axial momentum conservation equations and the energy conservation equation for an unsteady, incompressible, axisymmetric, turbulent flow are considered. The Standard k-ε turbulence model is accommodated to account for the turbulence. Moreover, the Species transport model is used to account for the mass transfer of the vapor jet from the cavity into the stagnant water ambient. It should be noted that all the unknown quantities are time-averaged since the RANS equations are being used.

Continuity Equation:

$$\frac{1}{r}\frac{\partial(rV_r)}{\partial r} + \frac{\partial V_z}{\partial r} = 0 \tag{8}$$

Momentum Equations:

Radial momentum:

$$\frac{\partial(\rho V_r)}{\partial t} + \frac{1}{r}\frac{\partial(\rho r V_r^2)}{\partial r} + \frac{\partial(\rho V_r V_z)}{\partial z} = -\frac{\partial p}{\partial r} + \frac{2}{r}\frac{\partial}{\partial r}\left(\mu_{eff} r\frac{\partial V_r}{\partial r}\right) + \frac{\partial}{\partial z}\left(\mu_{eff}\frac{\partial V_r}{\partial z}\right) + \frac{\partial}{\partial z}\left(\mu_{eff}\frac{\partial V_z}{\partial z}\right) - 2\mu_{eff}\frac{V_r}{r^2} \tag{9}$$

Axial momentum:

$$\frac{\partial(\rho V_z)}{\partial t} + \frac{1}{r}\frac{\partial(\rho r V_r V_z)}{\partial r} + \frac{\partial(\rho V_z^2)}{\partial z} = -\frac{\partial p}{\partial z} + \frac{1}{r}\frac{\partial}{\partial r}\left(\mu_{eff} r\frac{\partial V_z}{\partial r}\right) + 2\frac{\partial}{\partial z}\left(\mu_{eff}\frac{\partial V_z}{\partial z}\right) + \frac{1}{r}\frac{\partial}{\partial r}\left(\mu_{eff} r\frac{\partial V_r}{\partial z}\right) \tag{10}$$

where,

$$\mu_{eff} = \mu + \mu_t : \mu_t = \frac{\rho C_\mu K^2}{\varepsilon} : C_\mu = 0.09$$

Energy Equation:

$$\frac{\partial(\rho E)}{\partial t} + \frac{1}{r}\frac{\partial(rV_r\rho E)}{\partial r} + \frac{\partial(V_z\rho E)}{\partial z} = \frac{1}{r}\frac{\partial}{\partial r}\left(rk_{eff}\frac{\partial T}{\partial r}\right) + \frac{\partial}{\partial z}\left(k_{eff}\frac{\partial T}{\partial z}\right) + \left[\frac{1}{r}\frac{\partial}{\partial r}\left(rh_{vapor}\left(\rho D + \frac{\mu_t}{Sc_t}\right)\frac{\partial Y_{vapor}}{\partial r}\right) + \frac{\partial}{\partial z}\left(h_{vapor}\left(\rho D + \frac{\mu_t}{Sc_t}\right)\frac{\partial Y_{vapor}}{\partial z}\right)\right] + \left[\frac{1}{r}\frac{\partial}{\partial r}\left(rh_{air}\left(\rho D + \frac{\mu_t}{Sc_t}\right)\frac{\partial Y_{air}}{\partial r}\right) + \frac{\partial}{\partial z}\left(h_{air}\left(\rho D + \frac{\mu_t}{Sc_t}\right)\frac{\partial Y_{air}}{\partial z}\right)\right] \tag{11}$$

where, $E = Y_{air}\, h_{air} + Y_{vapor}\, h_{vapor}$, after neglecting the contribution of kinetic energy. Enthalpy of vapor and air are

$$h_{vapor} = \int_{T_{ref}}^{T} Cp_{vapor}dT = Cp_{vapor}(T - T_{ref}) \tag{12}$$

$$h_{water} = \int_{T_{ref}}^{T} Cp_{water}dT = Cp_{water}(T - T_{ref}) \tag{13}$$

In Eq. 11, the properties and parameters are

$$k_{eff} = k + k_t : k_t = Cp\frac{\mu_t}{\mathrm{Pr}_t} \text{ and } D = 2.88\times10^{-5}(\mathrm{m}^2/\mathrm{s}) : Sc_t = 0.7 : \mathrm{Pr}_t = 0.85 : T_{ref} = 298.15\mathrm{K}$$

Turbulence Kinetic Energy Equation, K:

$$\frac{\partial(\rho K)}{\partial t} + \frac{1}{r}\frac{\partial(\rho r V_r K)}{\partial r} + \frac{\partial(\rho V_z K)}{\partial z} = \frac{1}{r}\frac{\partial}{\partial r}\left(\frac{\mu_{eff}}{\sigma_K} r\frac{\partial K}{\partial r}\right) + \frac{\partial}{\partial z}\left(\frac{\mu_{eff}}{\sigma_K}\frac{\partial K}{\partial z}\right) - \rho\varepsilon + P_K \tag{14}$$

where,

$$P_K = \mu_{\text{eff}}\left[2\left\{\left(\frac{\partial V_z}{\partial r}\right)^2+\left(\frac{\partial V_r}{\partial r}\right)^2+\left(\frac{V_r}{r}\right)^2\right\}+\left(\frac{\partial V_z}{\partial r}+\frac{\partial V_r}{\partial z}\right)^2\right]$$

Rate of Dissipation Equation, ε:

$$\frac{\partial(\rho\varepsilon)}{\partial t}+\frac{1}{r}\frac{\partial(\rho r V_r\varepsilon)}{\partial r}+\frac{\partial(\rho V_z\varepsilon)}{\partial z}=\frac{1}{r}\frac{\partial}{\partial r}\left(\frac{\mu_{\text{eff}}}{\sigma_\varepsilon}r\frac{\partial\varepsilon}{\partial r}\right)+\frac{\partial}{\partial z}\left(\frac{\mu_{\text{eff}}}{\sigma_\varepsilon}\frac{\partial\varepsilon}{\partial z}\right)-C_1\frac{\varepsilon}{K}P_K-C_2\rho\frac{\varepsilon^2}{K} \quad (15)$$

where,

$$P_K = \mu_{\text{eff}}\left[2\left\{\left(\frac{\partial V_z}{\partial r}\right)^2+\left(\frac{\partial V_r}{\partial r}\right)^2+\left(\frac{V_r}{r}\right)^2\right\}+\left(\frac{\partial V_z}{\partial r}+\frac{\partial V_r}{\partial z}\right)^2\right]$$

and

$$\sigma_K = 1, \qquad \sigma_\varepsilon = 1.3, \qquad C_1 = 1.44, \qquad C_2 = 1.92$$

Species Transport Equation:

$$\frac{\partial(\rho Y_{\text{vapor}})}{\partial t}+\frac{1}{r}\frac{\partial(rV_r\rho Y_{\text{vapor}})}{\partial r}+\frac{\partial(V_z\rho Y_{\text{vapor}})}{\partial z}=\left[\frac{1}{r}\frac{\partial}{\partial r}\left(r\left(\rho D+\frac{\mu_t}{Sc_t}\right)\frac{\partial Y_{\text{vapor}}}{\partial r}\right)+\frac{\partial}{\partial z}\left(\left(\rho D+\frac{\mu_t}{Sc_t}\right)\frac{\partial Y_{\text{vapor}}}{\partial z}\right)\right] \quad (16)$$

where $Y_{\text{air}} = 1 - Y_{\text{vapor}}$.

Initial and Boundary Conditions:

Figure 10 shows the solution domain.

Symmetry Axis: ($r = 0$)

At the symmetry axis all the unknown quantities are considered to be maximum accept the r-direction velocity, which is zero.

$$\left.\frac{\partial V_z}{\partial r}\right|_{\substack{z=z\\r=0}} = 0 : V_r(z,0) = 0 : \left.\frac{\partial T}{\partial r}\right|_{\substack{z=z\\r=0}} = 0 : \left.\frac{\partial K}{\partial r}\right|_{\substack{z=z\\r=0}} = 0 : \left.\frac{\partial\varepsilon}{\partial r}\right|_{\substack{z=z\\r=0}} = 0 : \left.\frac{\partial Y_{\text{vapor}}}{\partial r}\right|_{\substack{z=z\\r=0}} = 0$$

Outflow: (At $z = 0$)

At the outflow boundary perpendicular to the z-axis the normal derivatives of all the unknown quantities are considered to be zero accept the r-direction velocity, whose value is zero as required from the continuity equation.

$$\left.\frac{\partial V_z}{\partial z}\right|_{\substack{z=0\\r=r}} = 0 : V_r(0,r) = 0 : \left.\frac{\partial T}{\partial z}\right|_{\substack{z=0\\r=r}} = 0 : \left.\frac{\partial K}{\partial r}\right|_{\substack{z=0\\r=r}} = 0 : \left.\frac{\partial\varepsilon}{\partial r}\right|_{\substack{z=0\\r=r}} = 0 : \left.\frac{\partial Y_{\text{vapor}}}{\partial r}\right|_{\substack{z=0\\r=r}} = 0$$

Outflow: (At $r = r_{\max}$)

At the outflow boundary perpendicular to the r-axis the normal derivatives of all the unknown quantities are considered to be zero accept the z-direction velocity, whose value is zero as required from the continuity equation.

$$V_z(z,r_{\max}) = 0 : \left.\frac{\partial V_r}{\partial r}\right|_{\substack{z=z\\r=r_{\max}}} = 0 : \left.\frac{\partial T}{\partial r}\right|_{\substack{z=z\\r=r_{\max}}} = 0 : \left.\frac{\partial K}{\partial r}\right|_{\substack{z=z\\r=r_{\max}}} = 0 : \left.\frac{\partial\varepsilon}{\partial r}\right|_{\substack{z=z\\r=r_{\max}}} = 0 : \left.\frac{\partial Y_{\text{vapor}}}{\partial r}\right|_{\substack{z=z\\r=r_{\max}}} = 0$$

Solid Wall: $z = f(r, t)$

The surface of the substrate material including the cavity wall acts like a wall in the solution domain and hence a no-slip and no-temperature jump boundary conditions are considered. At the cavity surface, the vapor mass fraction is considered to be one whereas the water mass fraction is considered to be zero. In this case, the function $f(r, t)$ defining the cavity wall shape, as obtained from the heat transfer analysis, can be presented in algebraic form, i.e.

$$f(r,t) = \left[c\left((r/\Delta r)^2 - r_{\max}^2\right)+d\left((r/\Delta r)^3 - r_{\max}^3\right)\right](\rho_l/\rho_v)\Delta z$$

where $c = cc_3 + cc_2(t/\Delta t) + cc_1(t/\Delta t)^2$

$cc_1 = 4.4499\times10^{-6} : cc_2 = -0.0026726 : cc_3 = -0.15077$

and $d = cd_3 + cd_2(t/\Delta t) + cd_1(t/\Delta t)^2$

$cd_1 = -1.7974\times10^{-7} : cd_2 = 0.00011187 : cd_3 = 0.0062477$

and $r_{\max} = cr_5 + cr_4(t/\Delta t) + cr_3(t/\Delta t)^2 + cr_2(t/\Delta t)^3 + cr_1(t/\Delta t)^4$

$cr_1 = -2.5982\times10^{-9} : cr_2 = 2.0455\times10^{-6} : cr_3 = -0.00059955 : cr_4 = 0.086871 : cr_5 = 7.7763$

$$\Delta z = 3.2415\times10^{-8}\ \text{m}$$

$$\Delta r = 8.3333\times10^{-8}\ \text{m}$$

The recession velocity of the cavity wall as obtained from the previous section can be represented in the algebraic form. In this case, the cavity size is limited with $0 \le r \le r_{\max}$. Therefore, the recession velocity of the cavity along the vertical direction is

$$V_z(f(r,t),r) = \frac{\rho_l}{\rho_v}\frac{\partial f}{\partial t}\frac{\partial f/\partial r}{\sqrt{1+(\partial f/\partial r)^2}}, \quad 0 \le \text{r} \le \text{r}_{\max}$$

Moreover, out side of the cavity a stationary solid wall is considered (Figure 4a). The recession velocity along the vertical axis is, therefore

$$V_z(f(r,t),r) = 0, \quad r > r_{\max}$$

The recession velocity of the cavity along the radial direction is

$$V_r(f(r,t),r) = \frac{\rho_l}{\rho_v}\frac{\partial f}{\partial t}\frac{1}{\sqrt{1+(\partial f/\partial r)^2}}, \quad 0 \le r \le r_{\max}$$

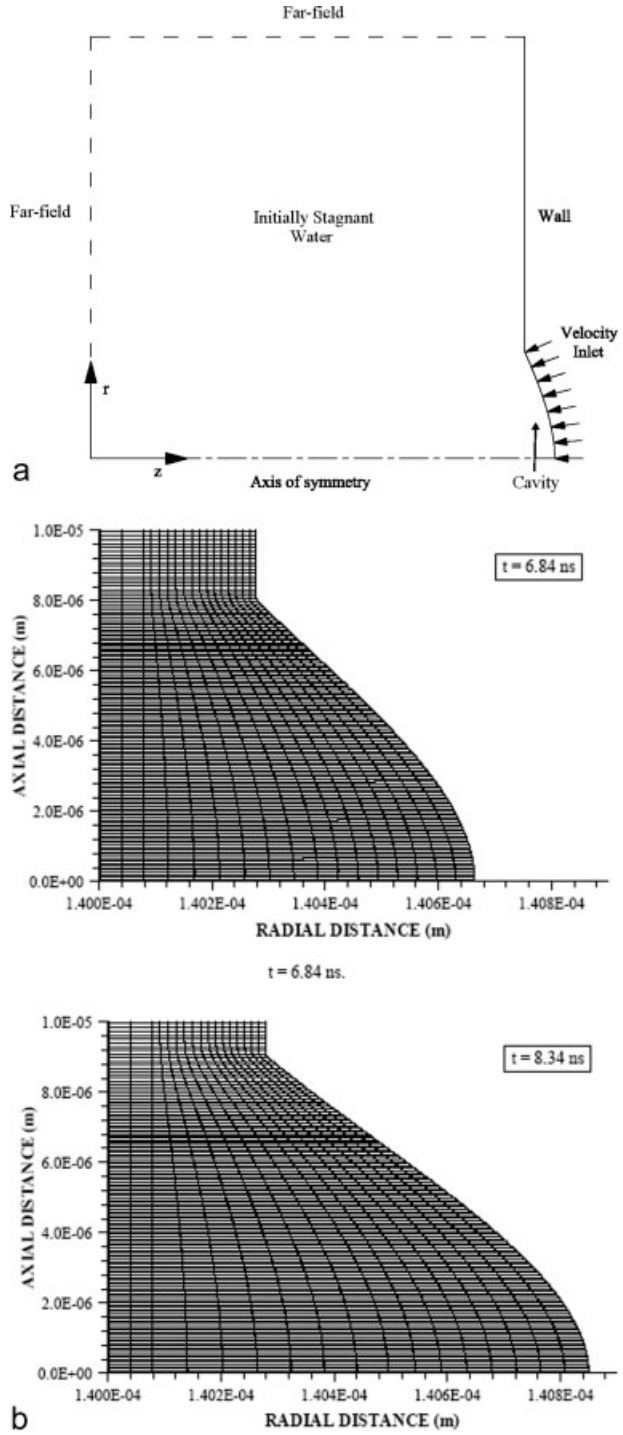

Figure 4. (a) Solution domain for an axisymmetric transient turbulent vapor jet emanating from the cavity and emerging into initially stagnant water; (b) a closed view of a moving mesh used in the cavity during the simulations.

Outside of the cavity a stationary solid wall is considered (Figure 4a). The recession velocity along the radial direction is, therefore

$$V_r(f(r,t),r) = 0, \quad r > r_{\max}$$

Temperature at the cavity wall is determined from the previous section and can be presented in algebraic form. In this case, temperature at the cavity wall is the same as the boiling temperature of the substrate material (T_b), i.e.

$$T(f(r,t),r) = T_b, \quad 0 \le r \le r_{\max}$$

$$T(f(r,t),r) = 2834\exp\left(-\text{btemp}((r/\Delta r) - r_{\max})^2\right) + 300, \quad r > r_{\max}$$

$$\text{btemp} = \text{ctemp}(t/\Delta t)^2 + \text{dtemp}(t/\Delta t) + \text{etemp}$$

$$\text{ctemp} = 1.0370442955011 \times 10^{-6}$$

$$\text{dtemp} = -3.39682806506743 \times 10^{-5}$$

$$\text{etemp} = 0.0241815719639816$$

Turbulence kinetic energy and dissipation of the jet in the cavity wall region is assumed to be constant and taken as

$$K(f(r,t),r) = 1(\text{m/s})^2$$

$$\varepsilon(f(r,t),r) = 1(\text{m/s})^2$$

$$Y_{\text{vapor}}(f(r,t),t) = 1, \quad 0 \le r \le r_{\max}$$

$$Y_{\text{vapor}}(f(r,t),r) = 0, \quad r > r_{\max}$$

Initial Conditions:

Initially, the ambient water is assumed as stagnant; therefore the z- and r-direction velocity components are zero. The temperature is considered to be uniform and equal to 300 K in water ambient. Initially, the vapor mass fraction is zero whereas the water mass fraction is one throughout the domain.

$$V_z(z,r) = 0 : V_r(z,r) = 0 : T(z,r) = 300\ \text{K} : K(z,r) = 1$$

$$\varepsilon(z,r) = 1 : Y_{\text{vapor}}(z,r) = 0$$

Numerical Solution

Phase change process

Equation 1 is applicable to solid and liquid heating, Eq. 6 is applicable to mushy zone at solid-liquid interface and Eq. 7 is applicable to mushy zone at liquid-vapor interface. To discretize the governing equations, a finite difference scheme is introduced. The details of the numerical scheme are given in.[15] To compute the equations discretized for temperature field and relative positions of solid-liquid and liquid-vapor interface, an implicit scheme is used, i.e., using the initial conditions, the temperature in the whole domain is calculated for following time steps with the respective conditions.

The calculation domain is divided into grids as shown in Figure 3 and grid independence test is being performed for different grid size and orientation. The grid size resulting

Table 1. Thermal Properties of Steel Used in the Simulations

T_m (K)	T_m (K)	ρ (kg/m^3)	Cp (J/kg/K)	k (W/m/K)	δ (1/m)	L_m (J/kg)	L_b (J/kg)
1811	3134	7860	420	63	6.17×10^6	247,112	6,213,627

grid independent solution is used, which is 120 × 120 points. A computer program based on implicit scheme is developed to compute the temperature field.

The material properties and pulse intensity used in the simulations are given Tables 1–3, respectively. It should be noted that the laser pulse properties employed in the simulations resemble the actual pulse used in the experiment (Figure 1).

Transiently Developing Jet

A control volume approach is employed when discretizing the governing equations and the discretization procedure is given in Ref. 16. A staggered grid arrangement is used in which the velocities are stored at a location midway between the grid points, i.e., on the control volume faces. All other variables including pressure are calculated at the grid points. This arrangement gives a convenient way of handling the pressure linkages through the continuity equation and is known as semi-implicit method for pressure-linked equations (SIMPLE) algorithm. The details of this algorithm are given in Ref. 16.

The computer program used for the present simulation can handle a nonuniform grid spacing. Along the radial direction, fine uniform grid spacing is allocated at the inlet (in cavity symmetry axis region) while gradually increasing spacing is considered away from the inlet (in the cavity edge region). Along the axial direction, again fine uniform grid spacing is used inside and near the cavity while the grid spacing gradually increases away from the cavity. The number of grid points in the radial direction is 300 while 215 grid points are used in the axial direction. Since the problem is involved with the moving boundary, the moving meshes are accommodated in the cavity to account for the cavity recession with time. The solution domain is shown in Figure 4a while the computational moving grid used in the cavity is shown in Figure 4b for two times. The grid independence test result for velocity is shown in Figure 5. It maybe observed that for 215 × 300, 265 × 300, 265 × 370, and 265 × 370 grid points the results are almost in agreement.

Eight variables are computed at all grid points. These are the two velocity components, local pressure, two turbulence quantities, temperature, and two mass fractions.

Table 2. Properties of Water and Water-Vapor Used in the Simulations

	Water	Water-Vapor
Density (kg/m^3)	998.2	50,800
Viscosity (kg/m/s)	0.001003	1.34×10^{-5}
Mass diffusivity (m^2/s)	2.88×10^{-5}	
Specific heat capacity (J/kg/K)	4182	2014
Thermal conductivity (W/m/K)	0.6	0.0261
Molecular weight (kg/kg mol)	18.0152	18.015

Results and Discussions

The formation of cavity due to high intensity laser irradiation and the flow field due to jet emanating from a laser produced cavity are considered. The cavity shape, velocity, pressure, and temperature fields in the evaporating front are predicted numerically. Since the cavity formation is transient, a transient moving boundary problem is accommodated in the analysis. Laser produced cavity is assumed to be formed in the water ambient. This is the situation where the laser induced shock processing being carried out. Consequently, the vapor emanating from the cavity expands into the water ambient. Since the thermophysical properties of the vapor front are not known and the equation of state for laser produced vapor is not formulated, a density of vapor front is assumed. In addition, due to unknown equation of state for the vapor phase, the vapor front is assumed to be incompressible. Moreover, as the cavity recesses with time, the vapor-liquid front recesses with the same recession velocity of the cavity towards the solid bulk. The selection of vapor front density is made about 1/10 time of the liquid density.[17]

Figure 6 shows three-dimensional view of laser produced cavity inside the substrate material for different heating periods while Figure 7 shows the cross-sectional view of the cavity formed at different heating periods, i.e., the liquid-vapor and solid-liquid mushy zones as well as liquid and solid zones are shown. The cavity size gradually increases after 19.5 ns, and then it remains almost the same with progressing time. This is because of the laser beam energy which reduces gradually with time after 20 ns of the heating duration (Figure 1b). In the case of Figure 7, the mushy zone at liquid-vapor interface is thicker than the mushy zone at solid-liquid interface for all heating periods. This is because of the latent heat of evaporation, which is considerably higher than the latent heat of fusion (Table 1). Moreover, the liquid layer thickness remains almost uniform along the radial direction in the early heating period (t = 6.54 ns). As the heating period progresses, the liquid layer thickness becomes large towards the edge of the cavity in the radial direction, particularly for the heating period corresponding to the high power intensity (10.92 ns $\leq t \leq$ 15.23 ns). In this case, high power intensity in the region of the symmetry axis enhances the evaporation rate and the liquid phase evaporates at a high rate reducing the liquid layer thickness in this region. Moreover, the thickness of the mushy zone at liquid-vapor interface reduces significantly as the heating period progresses. This indicates that in the region of the high

Table 3. Laser Pulse Intensity Used in the Simulations

Peak Intensity (W/m^2)	Gaussian Parameter (1/m)	Nominal Pulse Length (ns)
8×10^{12}, 9×10^{12}, 1×10^{13}	120,000	24

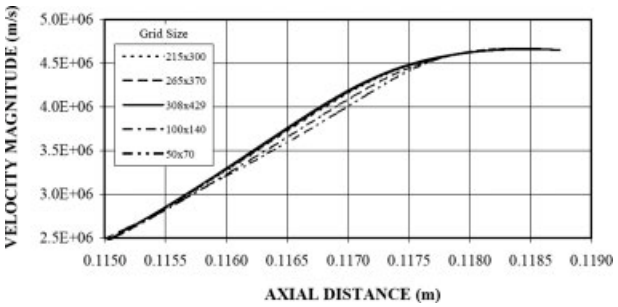

Figure 5. Grid independence test for velocity magnitude along the symmetry axis.

intensity, the size of the mushy zone at liquid-vapor interface becomes small. It should be noted that the heating duration is short (few nanoseconds) and the liquid layer thickness is small (fraction of micrometer); therefore, liquid flow in the cavity can be neglected and the effects of liquid motion on the heat transfer characteristics are negligible in the cavity during nanoseconds of heating duration.

Figure 8 shows the velocity contours in and around the cavity for three heating periods. It should be noted that the evaporation takes place after 1.8 ns from the laser pulse initiation. In the early heating period (t = 6.54 ns), jet expansion is more

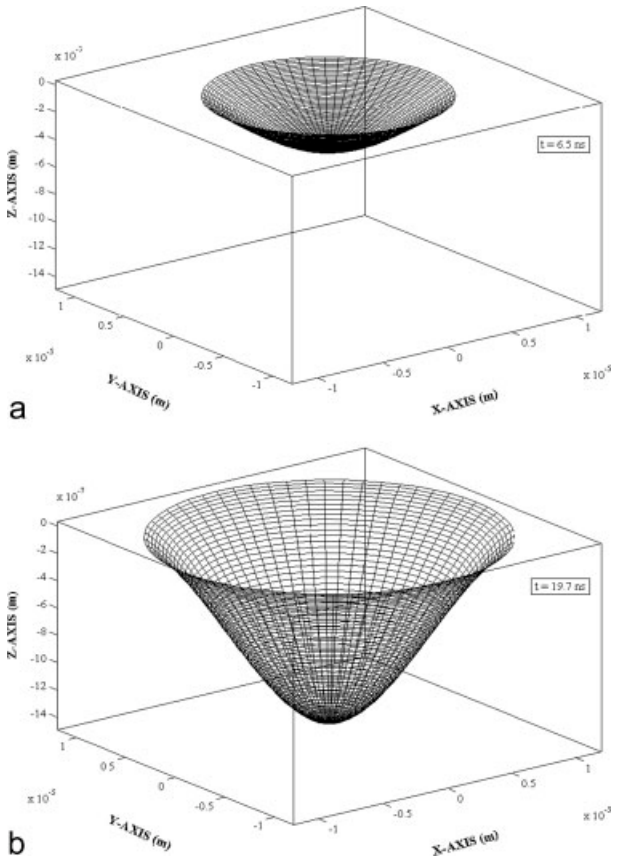

Figure 6. Three-dimensional view of the cavity at two different time durations.

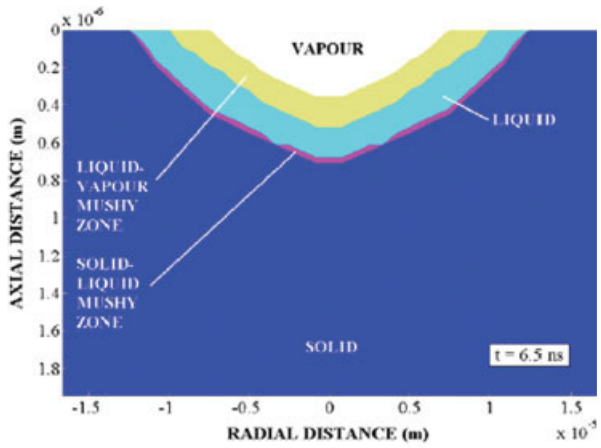

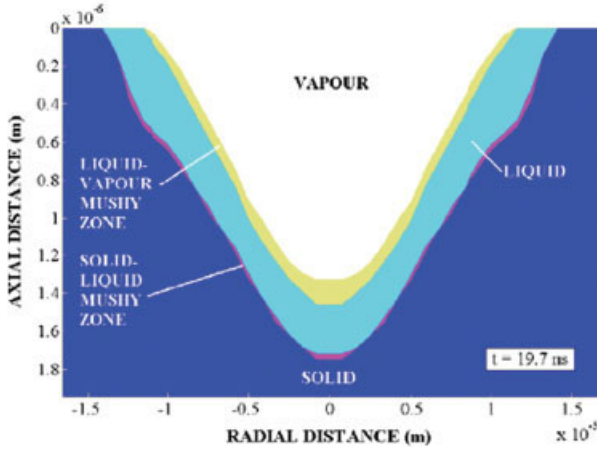

Figure 7. Cross-sectional view of cavity for two different heating periods.

[Color figure can be viewed in the online issue, which is available at www.interscience.wiley.com.]

pronounced in the axial direction provided that the cavity diameter is small at cavity exit. The abrupt expansion of the jet into the stagnant ambient results in flow disturbance around the jet boundary. However, this expansion cannot generate a circulation cell next to the jet boundary i.e., it is the ambient density, which is high, suppressing the circulation cell next to the jet boundary. Moreover, decay of radial momentum of the jet also contributes the suppression of the circulation in this region. As the heating period progresses, jet expansion in the radial direction enhances, particularly in the front region of the jet. This can be observed from the velocity contour of 3.2×10^2 m/s. Temporal extension of the velocity contour is more pronounced in the radial direction when comparing the jet behavior at time durations of 7.74 and 8.34 ns. In this case, jet produced from the cavity remains almost at the same velocity. The high density fluid suppresses the axial velocity due to momentum conservation and radial velocity increases at the jet frontal region.

Figure 9 shows pressure contours in the jet for different heating durations. In the early heating period (t = 6.54 ns), pressure is build up in the cavity and the decay in radial momentum in the vicinity of the cavity results in high pressure generation in this region. This is particularly true for late heating periods. Pressure in the cavity reaches extremely high

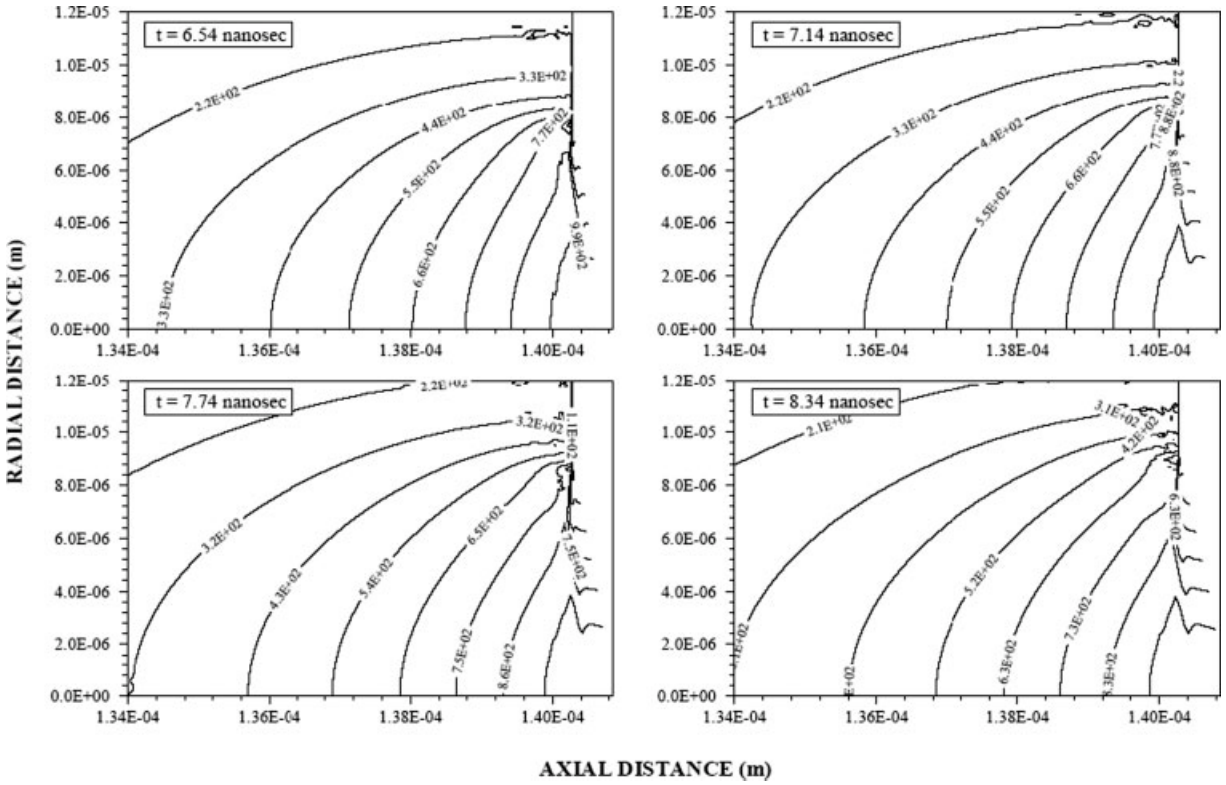

Figure 8. Contour plots of velocity magnitude for different heating durations in region of cavity exit.

magnitude in the early heating period and as the heating progresses, jet production in the cavity enables the axial expansion of jet. This, in turn, lowers the pressure in the cavity. Although the center of high pressure region is formed towards the edge of the cavity, axial expansion of the jet is not affected by this pressure center. It should be noted that the recession of the

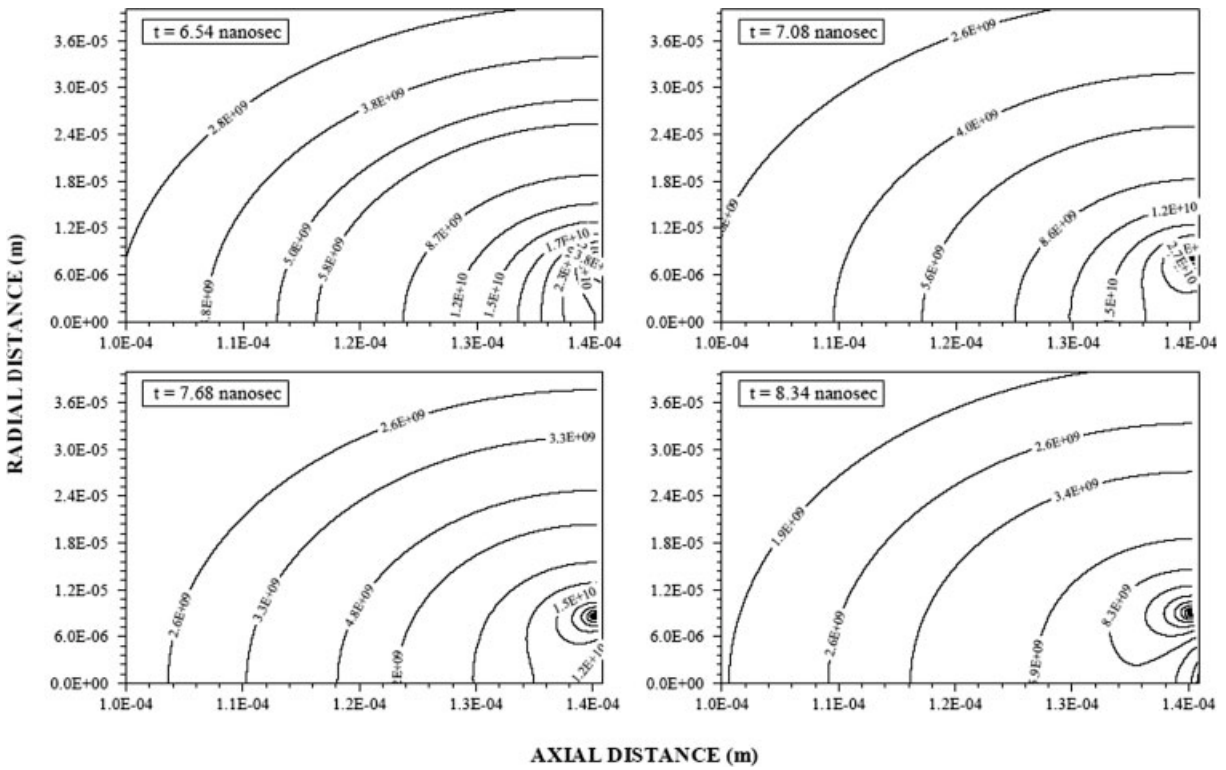

Figure 9. Contour plots of pressure for three different heating durations in the region of cavity exit.

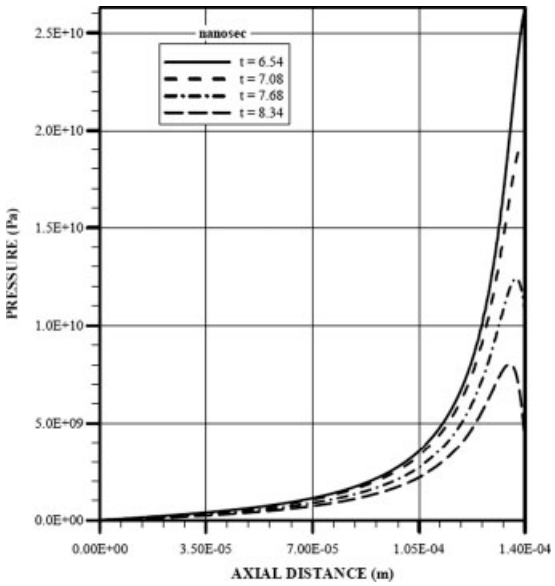

Figure 10. Pressure variation along the symmetry axis for different heating durations.

cavity with time develops complex flow field in the cavity. However, at the outer edge of the jet, the flow behavior is controlled by the high density fluid surrounding the jet. The magnitude of pressure in the cavity reaches as high as 10 GPa.

Figure 10 shows pressure variation along the symmetry axis for different heating periods. The location of maximum pressure along the symmetry axis occurs away from the cavity wall. This is because of the recession of the cavity surface with time, i.e., cavity wall recesses opposite to the jet expansion creating the suction in the region of the cavity wall. This, in turn, lowers the pressure in this region. However, in the early heating period the cavity recession is less and the pressure builds up in the cavity. This results in excessive pressure generation in this region. This can also be observed from Figure 11, in which maximum pressure along the symmetry axis is shown. The radial expansion of the jet in the jet frontal region reduces the pressure in the jet in this region. Consequently, jet expansion in the radial direction with progressing time results in decay of pressure in the jet.

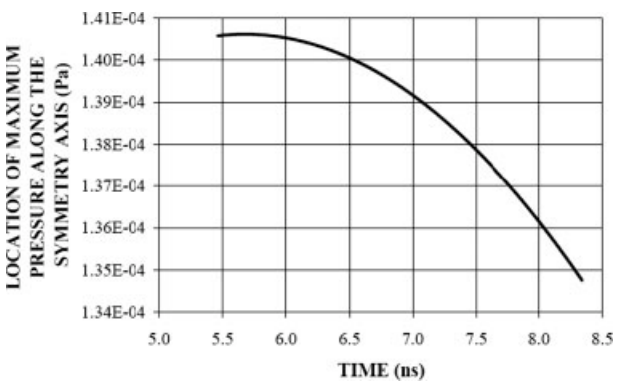

Figure 11. Location of maximum pressure at different heating periods.

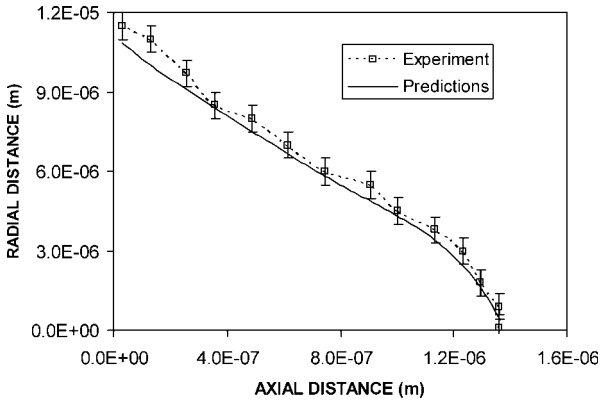

Figure 12. Cavity shape predicted from the experiment and obtained from the experiment for a single pulse irradiation.

Figure 12 shows the cavity shape obtained from predictions and the experiment. It should be noted that the laser power intensity distribution (temporal and spatial) used in the experiment was measured and employed in the simulations. It can be observed that the cavity profile predicted from the model agrees well with the experimental data. Figure 13 shows the recession velocity predicted and obtained from the previous analytical formulation.[18] The recession velocity predicted and obtained from the previous analytical formulation are in agreement. Moreover, some small discrepancies between both results are due to the one-dimensional consideration in the previous formulation. Consequently, the radial heat diffusion, which was omitted in the analytical solution, results in small changes in the recession velocity.

Conclusion

Laser heating of steel surface is considered and phase change processes during the heating pulse are modeled. The cavity formation and recession velocity of the solid surface are predicted. A finite difference scheme is used to descritize

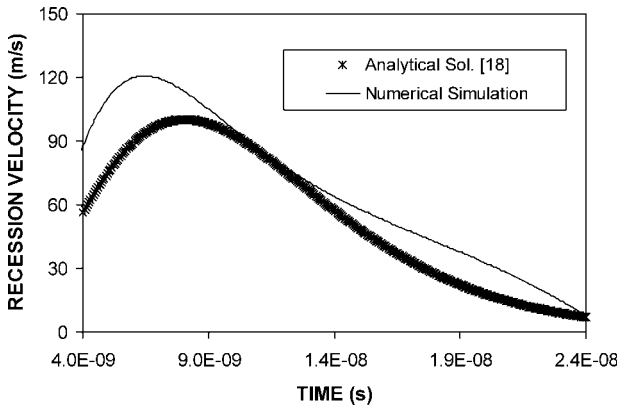

Figure 13. Comparison of recession velocity obtained from present predictions along the symmetry axis and one-dimensional analytical solution.[18]

three-dimensional governing equations of heat transfer. The predictions are compared with the experimental results. An evaporating front jet emerging of a laser produced cavity is considered and a numerical method employing a control volume is accommodated to predict the flow characteristics. A moving mesh is employed to account for the transiently moving boundary problem due to cavity recession. Laser pulse shape resembling the actual laser pulse used in the experiment is accommodated in the simulations. It is found that the size of mushy zone changes with time and space, provided that the size of the cavity change becomes insignificant as the heating period progresses further $t > 19.5$ ns, which is due to the temporal variation of laser pulse heating. The recession velocity of the evaporating surface is higher in the region close to the symmetry axis than that corresponding to the region close to the edge of the irradiated spot. The prediction of cavity shape agrees well with the experimental result.

The jet expansion in the axial direction is significant in the early heating period and radial expansion, particularly in the jet frontal area is evident as the heating period progresses. This is due to the ambient fluid above the cavity exit, which has higher density than the jet, i.e., it suppresses the axial extension of the jet particularly at long durations. The recoil pressure developed in the cavity is considerably high, particularly in the region close to the cavity edge; however, as time progresses, it reduces in the vicinity of the cavity due to cavity recession. The cavity profiles predicted from the model and experiment are in a good agreement.

Acknowledgments

The authors acknowledge the support of King Fahd University of Petroleum and Minerals. Dhahran, Saudi Arabia for this work.

Notation

a: = Gaussian parameter (m)
A = area (m^2)
a = Gaussian parameter (m)
C_p = specific heat capacity (J/kg/K)
C = various empirical constants in turbulence model
$cp_{1,2,3,4,5}$ = coefficients in the source term
D = species diffusion coefficient (m^2/s), jet width (m)
F_j = mass flux through the face 'j' (kg/s/m^2)
$F_{e,w,n,s}$ = mass flow rate through faces of the control volume (kg/s)
$f(r, t)$ = cavity profile equation
h = convective heat transfer coefficient (W/m^2/K); Sensible enthalpy (J/kg)
I_o = laser power intensity (W/m^2)
J_j = total flux (convection plus diffusion) across face 'j' (kg/s/m^2 $\times$ [φ])
K = turbulence kinetic energy (m^2/s^2)
k = thermal conductivity (W/m/K)
k_t = turbulent thermal conductivity (W/m/K)
L = latent heat (J/kg)
Pr = Prandtl number
$\bar{p}$ = time-averaged pressure (Pa)
p' = fluctuating component of mixture pressure (Pa)
$\bar{p}'$ = pressure correction (Pa)
r = distance along the radial direction (m)
r_f = reflectance
S = source term (W/m^3)
Sc = Schmidt number
T = temperature (K)
$\bar{T}$ = time-averaged temperature (K)
T' = fluctuating component of temperature (K)
t = time (s)
t_m = time at which melting starts in the solid phase (s)
t_{sl} = time at which solid-liquid mushy zone starts converting into the liquid phase (s)
t_b = time at which evaporation starts in the liquid phase (s)
U = energy content (J)
u = velocity component (m/s), z- direction velocity (m/s)
$\bar{u}$ = time-averaged velocity component (m/s), Time-averaged z-direction velocity (m/s)
u' = fluctuating component of z-direction velocity (m/s)
$\bar{u}'$ = z-direction velocity correction (m/s)
$\bar{u}^*$ = guessed z-direction velocity (m/s)
V = volume (m^3)
V = velocity (m/s)
v = r-direction velocity (m/s)
$\bar{v}$ = time-averaged r-direction velocity (m/s)
v' = fluctuating component of r- direction velocity (m/s)
$\bar{v}'$ = r-direction velocity correction (m/s)
$\bar{v}^*$ = guessed z-direction velocity (m/s)
x = quality
Y = mass fraction in species transport model
$\bar{Y}$ = time-averaged mass fraction in species transport model
zc = depth of cavity (m)
z = distance along the radial direction (m)

Greek letters

δ = reciprocal of absorption depth (m^{-1})
ε = rate of dissipation (m^2/s^3)
Γ = diffusion coefficient (kg/m/s)
μ = molecular viscosity coefficient (kg/m/s)
μ_t = turbulent viscosity coefficient (kg/m/s)
φ = arbitrary variable
[φ] = unit of arbitrary variable φ
ρ = density (kg/m^3)
$\bar{\rho}$ = time-averaged density (kg/m^3)
ρ' = fluctuating component of density (kg/m^3)
σ_K = turbulent Prandtl number for K
σ_ε = turbulent Prandtl number for ε

Subscripts

b = vapor-liquid mushy zone; boiling
eff = effective
l = liquid
max = maximum; maximum cavity radius
m = solid-liquid mushy zone; melting
o = initial value
p = time index
ref = reference
s = solid, surface
t = turbulent
v = vapor

Literature Cited

1. Dabby FW, Paek U. High-intensity laser-induced vaporization and explosion of solid material. *IEEE J Quant Electron.* 1972;QE-8:106–111.
2. Beck M, Berger P, Hugel H. The effect of plasma formation on beam focusing in deep penetration welding with CO_2 lasers. *J Phys D: Appl Phys.* 1995;28:2430–2442.
3. Lacroix D, Jeandel G, Boudot C. Spectroscopic characterisation of laser-induced plasma created during welding with a pulsed Nd:YAG laser. *J Appl Phys.* 1997;81:6599–6606.
4. Liu CL, Leboeuf JN, Wood RF, Geobegan DB, Donato JM, Chen KR, Puretzky AA. Computational modelling of physical processes during laser ablation. *Mater Sci Eng B.* 1997;47:70–77.

5. Semak V, Matsunawa A. The role of recoil pressure in energy balance during laser material processing. *J Phys D: Appl Phys*. 1997;30:2541–2552.
6. Szymanski Z, Kurzyna J, Kalita W. The spectroscopy of the plasma plume induced during laser welding of stainless steel and titanium. *J Phys D: Appl Phys*. 1997;30:3153–3162.
7. Zhang Y, Faghri A. Vaporization, melting and heat conduction in the laser drilling process. *Int J Heat Mass Transfer*. 1999;42:1775–1790.
8. Gusarov AV, Gnedovets AG, Smurov I. Two-dimensional gas-dynamic model of laser ablation in an ambient gas. *Appl Surf Sci*.200;154/155:66–72.
9. Kouros H, Medina R, Johari H. Spreading rate of an unsteady turbulent Jet. *AIAA J*. 1993;31:1524–1526.
10. Abraham J. Entrainment characteristics of transient gas jets. *Numer Heat Transfer A*. 1996;30:347–364.
11. Riopelle G, Stubley GD, Strong AB. Numerical study of the influence of the ambient pressure field on free plane turbulent vertical jets and plumes. *Numer Heat Transfer A*. 1994;26:273–286.
12. Ouellette P, Hill PG. Turbulent transient gas injections. *J Fluids Eng*. 2000;122:743–753.
13. Shuja SZ, Yilbas BS, Budair MO. Modeling of laser heating of solid substance including assisting gas impingement. *Numer Heat Transfer A*. 1998;33:315–339.
14. Blackwell FJ. Temperature profile in semi-infinite body with exponential source and convective boundary conditions. *ASME J Heat Transfer*. 1990;112:567–571.
15. Naqavi IZ. Conduction and non-conduction limited laser heating process—mathematical simulation. M.Sc. Thesis, Mechanical Engineering, Department, KFUPM, 2001.
16. Patankar SV. *Numerical Heat Transfer*. New York: McGraw-Hill, 1980.
17. Yilbas BS, Davies R, Yilbas Z, Gorur A, Acar I. Surface line and plug flow models governing laser produced vapor from metallic surfaces. *Pramana J Phys*. 1992;38:195–209.
18. Kalyon M, Yilbas BS. Analytical solution for laser evaporative heating process: time exponentially decaying pulse case. *J Phys D: Appl Phys*. 2001;34:3303–3311.

Manuscript received Mar. 9, 2007, revision received Sept. 29, 2007, and final revision received Nov. 29, 2007.